# An intense traveling airglow front in the upper mesosphere–lower thermosphere with characteristics of a bore observed over Alice Springs, Australia, during a strong 2 day wave episode

R. L. Walterscheid,[1] J. H. Hecht,[1] L. J. Gelinas,[1] M. P. Hickey,[2] and I. M. Reid[3]

Received 27 March 2012; revised 19 September 2012; accepted 21 September 2012; published 17 November 2012.

[1] The Aerospace Corporation's Nightglow Imager observed a large step function change in airglow in the form of a traveling front in the OH Meinel (OHM) and $O_2$ atmospheric (O2A) airglow emissions over Alice Springs, Australia, on 2 February 2003. The front exhibited nearly a factor of 2 stepwise increase in the OHM brightness and a stepwise decrease in the O2A brightness. There was significant (~25 K) cooling behind the airglow fronts. The OHM airglow brightness behind the front was among the brightest for Alice Springs that we have measured in 7 years of observations. The event was associated with a strong phase-locked 2 day wave (PL/TDW). We have analyzed the wave trapping conditions for the upper mesosphere and lower thermosphere using a combination of data and empirical models and found that the airglow layers were located in a region of ducting. The PL/TDW-disturbed wind profile was effective in supporting a high degree of ducting, whereas without the PL/TDW the ducting was minimal or nonexistent. The change in brightness in each layer was associated with a strong leading disturbance followed by a train of weak barely visible waves. In OHM the leading disturbance was an isolated disturbance resembling a solitary wave. The characteristics of the wave train suggest an undular bore with some turbulent dissipation at the leading edge.

**Citation:** Walterscheid, R. L., J. H. Hecht, L. J. Gelinas, M. P. Hickey, and I. M. Reid (2012), An intense traveling airglow front in the upper mesosphere–lower thermosphere with characteristics of a bore observed over Alice Springs, Australia, during a strong 2 day wave episode, *J. Geophys. Res.*, *117*, D22105, doi:10.1029/2012JD017847.

## 1. Introduction

[2] There have been frequent instances of sudden brightening or dimming of the airglow layer that appear to propagate across the sky as fronts, sometimes described as walls [*Taylor et al.*, 1995a; *Hecht et al.* 1995; *Swenson et al.*, 1998; *Smith et al.*, 2003, 2005, 2006; *Batista et al.*, 2002; *Fechine et al.*, 2005, 2009; *Medeiros et al.*, 2005; *Narayanan et al.*, 2009; *Nielsen et al.*, 2006; *She et al.*, 2004; *Stockwell et al.*, 2006; *Brown et al.* 2004; *Scheer and Reisin*, 2010; *Li et al.*, 2007]. Such changes are common and the transition between conditions before and after the passage of the fronts can be quite rapid [*Taylor et al.*, 1995a, 1995b; *Zhang and Shepherd* 1999; *Swenson et al.*, 1998; *Dewan and Picard*, 1998; *Hecht et al.*, 1995; *Smith et al.*, 2003, 2005, 2006].

[3] Instances of frontal phenomena have been interpreted as internal undular bores [*Smith et al.*, 2003, 2005; *Dewan and Picard*, 1998; *Nielsen et al.*, 2006]. Undular bores are nonlinear high Froude number phenomena and can be regarded as the wave transition between different basic states [*Grimshaw et al.*, 2002]. Evidence of nonlinearity is a wave train with amplitude-ordered waves that propagate with different phase speed depending on their amplitude [*Lighthill*, 1978; *Dewan and Picard*, 1998; *Knupp*, 2006; *Rottman and Einaudi*, 1993; *Grimshaw et al.*, 2002].

[4] Bores generate excess energy at the transition and undular bores shed this energy by generating waves that carry energy backward relative to the moving front [*Lighthill*, 1978]. Bores may also shed the excess energy generated at the front by means of turbulent dissipation [*Lighthill*, 1978]. Bores for which this is the primary means of energy dissipation are known as turbulent bores. The existence of front-like behavior indicates a horizontally propagating ducted wave that has acquired maximum amplitude at its leading edge [*Dewan and Picard*, 1998; *Smith et al.*, 2003, 2005, 2006].

[5] In this study, we show evidence suggesting an isolated disturbance at the leading edge of a dramatic change in airglow brightness with weak trailing waves. The OHM and O2A airglow brightnesses behind the front were among the brightest for Alice Springs that we have measured in 7 years of observations. The evidence includes a high degree of

[1]Space Science Applications Laboratory, The Aerospace Corporation, Los Angeles, California, USA.
[2]Department of Physical Sciences, Embry-Riddle Aeronautical University, Daytona Beach, Florida, USA.
[3]School of Chemistry and Physics, University of Adelaide, Adelaide, South Australia, Australia.

Corresponding author: R. L. Walterscheid, Space Science Applications Laboratory, The Aerospace Corporation, MS 260, PO Box 92957, Los Angeles, CA 90009, USA. (richard.walterscheid@aero.org)


0148-0227/12/2012JD017847

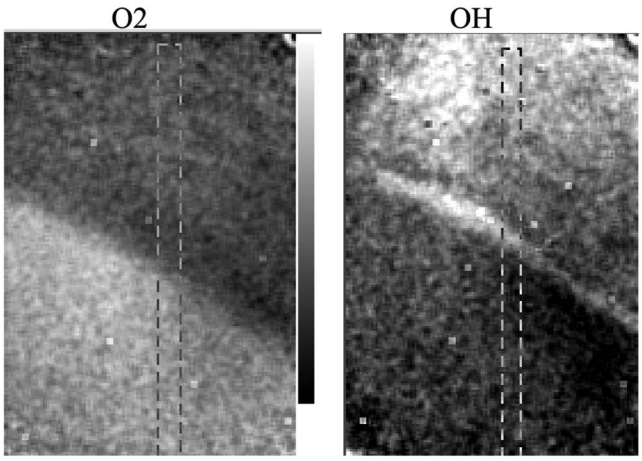


**Figure 1.** Image of (right) OHM brightness and (left) O2A brightness over Alice Springs showing a stepwise change in intensity moving across the image toward the lower left. The change is followed by an isolated disturbance with only a faint suggestion of a trailing wave train. The image size is 128 × 192 pixels (77 × 115 km).

ducting induced in large part by the Doppler ducting associated with a strong 2 day wave event, a sharp leading feature with trailing waves that travel slower than the leading wave and a large Froude number.

## 2. The Alice Springs Event

[6] In this section we describe an event resembling an undular bore with a large leading feature and weak trailing waves in the OH Meinel and $O_2$ Atmospheric airglow over Alice Springs, Australia (23.7°S, 133.9°E).

### 2.1. Measurements

[7] The airglow instrument at Alice Springs (AS), located at 23.8 S, 133.9 E, is a modified version of The Aerospace Corporation's charge coupled device (CCD) nightglow camera originally described by *Hecht et al.* [1994] and further described by *Hecht et al.* [2004]. The imager now uses a 1536 × 1024 Kodak CCD chip. The pixels are binned 8 × 8, resulting in images that have 192 × 128 pixels. Each pixel is 0.6 km on a side. The angular field of view is now 69 by 46 degrees giving a spatial field of view of approximately 122 × 75 km at 90 km altitude. This instrument obtains images of the OH Meinel (6,2) (hereinafter OHM) and $O_2$ Atmospheric (0,1) band (hereinafter O2A) band emissions. A sequence of five images is obtained, each at 1 min integration, through separate narrow passband filters. Two of the filters cover two different rotational lines of OHM, two filters cover different portions of O2A, and one filter covers the background and has almost no airglow emission in its passband. The latter is used to correct the airglow images for background skylight. Thus, one can obtain images of the OHM and O2A airglow, the intensity and temperature of the OHM and O2A emissions, and atmospheric gravity wave horizontal wavelengths and ground-based phase velocities [e.g., *Hecht et al.*, 1997, 2001]. For this work we discuss the OHM and O2A intensities and temperatures as determined using the techniques described by *Gelinas et al.* [2008].

### 2.2. Production of Airglow Temperature Images

[8] The imager employs five filters covering two rotational lines of the OH Meinel (6,2) emission, 8400 Å and 8430 Å, two rotational lines of the $O_2$ atmospheric (0,1) emission, 8660 Å and 8680 Å, and a background emission at 8750 Å. The exposure time for each filter is 60 s. A full set of measurements is taken every 7 min and includes two background images and a dark image. The filter sequence is BG (8750 Å), OH (8400 Å), OH (8430 Å), BG (8750 Å), O2 (8660 Å), O2 (8680 Å), DK.

[9] Temperatures near the peak of the OH emission altitude, near 87 km, were determined from the ratio of the 8400 Å to 8430 Å rotational lines. Images at each wavelength were first processed to remove dark counts, stars, and background contamination and then a flat-field correction was applied. Since the two images used to determine the temperature were separated in time by 1 min, the second image in the sequence was spatially shifted to account for bore motion between images (approximately 54 m $s^{-1}$). Temperatures near the peak of the O2A emission (94 km) are similarly determined using the ratio of 8660 Å to 8680 Å lines [e.g., *Hecht et al.*, 1994, 1997, 2004]. The results on a pixel by pixel basis were then averaged over a 100 pixel box. The RMS error per box was determined to be ∼2 K.

### 2.3. Airglow Brightness and Temperature Features

[10] In Figure 1 a distinct brightness front is observed in both airglow layers. In a sequence of such images, it is seen to move across the image in a direction ∼57.5° east of north (from the upper right to lower left of the image) at a speed of ∼54 m $s^{-1}$. The most distinct disturbance is a single narrow feature at the leading edge of the OHM image. There is also a weak trailing waveform.

[11] The boundary in both images separates regions with distinctly different levels of airglow brightness. In O2A (Figure 1, left) there is a decrease in the airglow brightness behind the wave, while in OHM (Figure 1, right) it is an increase. This is a common characteristic of waves reported as bores and is attributed to the fact that such waves must be ducted and can be associated with a node between layers [*Dewan and Picard*, 1998; *Walterscheid and Hickey*, 2009; *Snively et al.*, 2010].

[12] Figure 2 shows cuts across the image shown in Figure 1. The cuts are indicated by the vertical dashed lines in Figure 1. We see a large isolated feature separating regions with different airglow brightness. For OHM the disturbance is in the form of a large positive spike ∼10 pixels (6 km) across. For O2A the disturbance has the opposite sign and is somewhat broader being ∼30 pixels (18 km) across. The change in brightness behind the front relative to values ahead attains ∼40% of the mean for OHM and ∼20% for O2A. The change is far more step-like for O2A, the change in OHM taking the form of a steady increase after the front passes.

[13] Figure 3 shows the progression of the front in both images. Figure 3 shows two image sequences, one for O2A (Figure 3, top) and one for OHM airglow (Figure 3, bottom). There are two pairs of images in each emission 866 nm and 868 nm for O2A and 840 nm and 843 nm for OHM). Note that the time intervals are not equal. The time interval

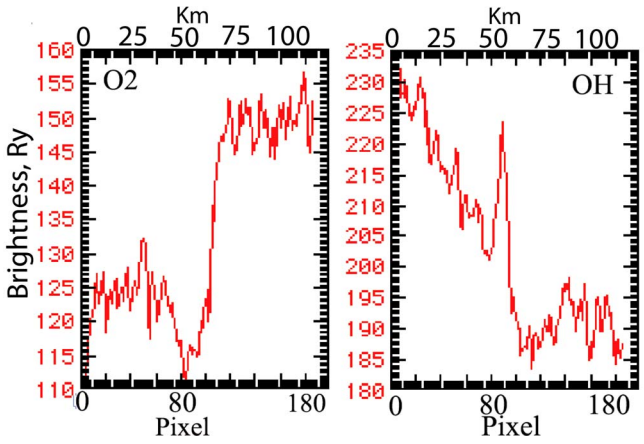


**Figure 2.** Brightness plots corresponding to dotted lines in Figure 1. Brightness is in rayleighs.

between members of a pair is 63 s. The time interval between pairs of the same emission is 7.3 min.

[14] Figure 4 shows a line plot of the O2A (Figure 4, left) and OHM brightness (Figure 4, right) integrated along a direction parallel to the wavefront. The brightness in two lines is shown for each of two emission bands at three different times for each band. The red and black curves in Figure 4 are separated by 63 s. The time between plots is 7.3 min. The wavefront is the large peak on the left. The waveform is propagating from right to left. The observations indicate a phase speed for the leading disturbance of ~54 m $s^{-1}$ and horizontal wavelength in the range 10–20 km. The tailing waves appear to be somewhat slower.

[15] The leading disturbance is by far the strongest with weaker trailing waves. The initial disturbance for OHM is a large isolated feature while for O2A it appears to be dispersed waveform with a single crest and trough. At the last time shown, the leading OHM disturbance is beginning to resemble a dispersed waveform. The distance between the initial OHM crest and the following one increases with time; the same is true for the second and third. There is no discernible amplitude ordering of the training waves.

[16] Figure 5 shows maps of O2A airglow temperature (Figure 5, top) and OHM temperature (Figure 5, bottom) sequences obtained from brightness pairs. A temperature front is seen corresponding approximately to the location of the airglow front. In both emissions, colder air is found behind the front than ahead. The change from the warmest temperature ahead of the front to the coldest temperatures behind is ~25 K in O2A and ~30 K in OHM. The differing temperature on either side of the moving front may be interpreted as a change in the basic state.

[17] A figure comparable to Figure 4 for temperature was not possible because of the larger uncertainties in the temperature determinations. To reduce noise levels, we examined the temperature averaged over the central 20 × 20 pixels (12 × 12 km) of the images. This gave a time history of the disturbance as it moved across the central part of the image with a time resolution of 7 min. The times series was further smoothed by means of a three-point average. Figure 6 shows a time history of the event as it passed the zenith. A rapid decrease of temperature in both layers commences shortly

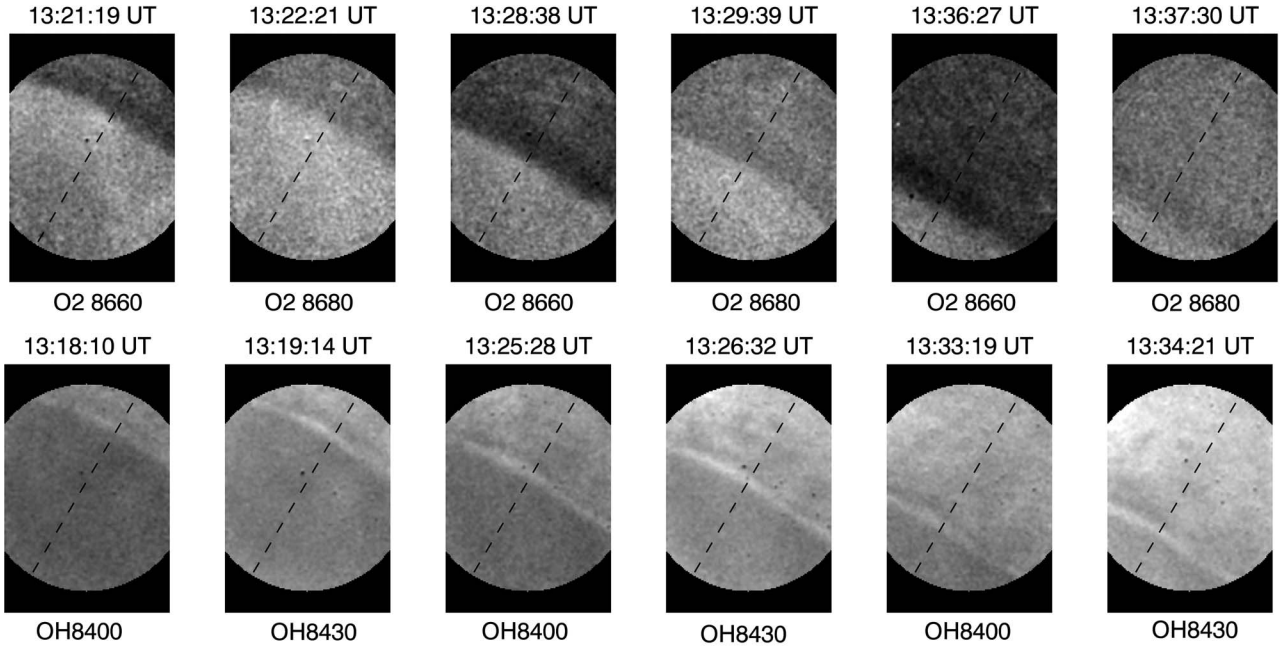


**Figure 3.** Image sequences for (top) $O_2$ and (bottom) OHM airglow showing the propagation of the front across the field of view of the imager. There are three pairs of images in each emission (866 nm and 868 nm for O2A and 840 nm and 843 nm for OHM). Note that the time intervals are not equal. The time interval between members of a pair is 63 s. The time interval between successive measurements of the same line is 7.3 min. The image size is 128 × 192 pixels (77 × 115 km). The black areas are where the image is masked to exclude edge effects.

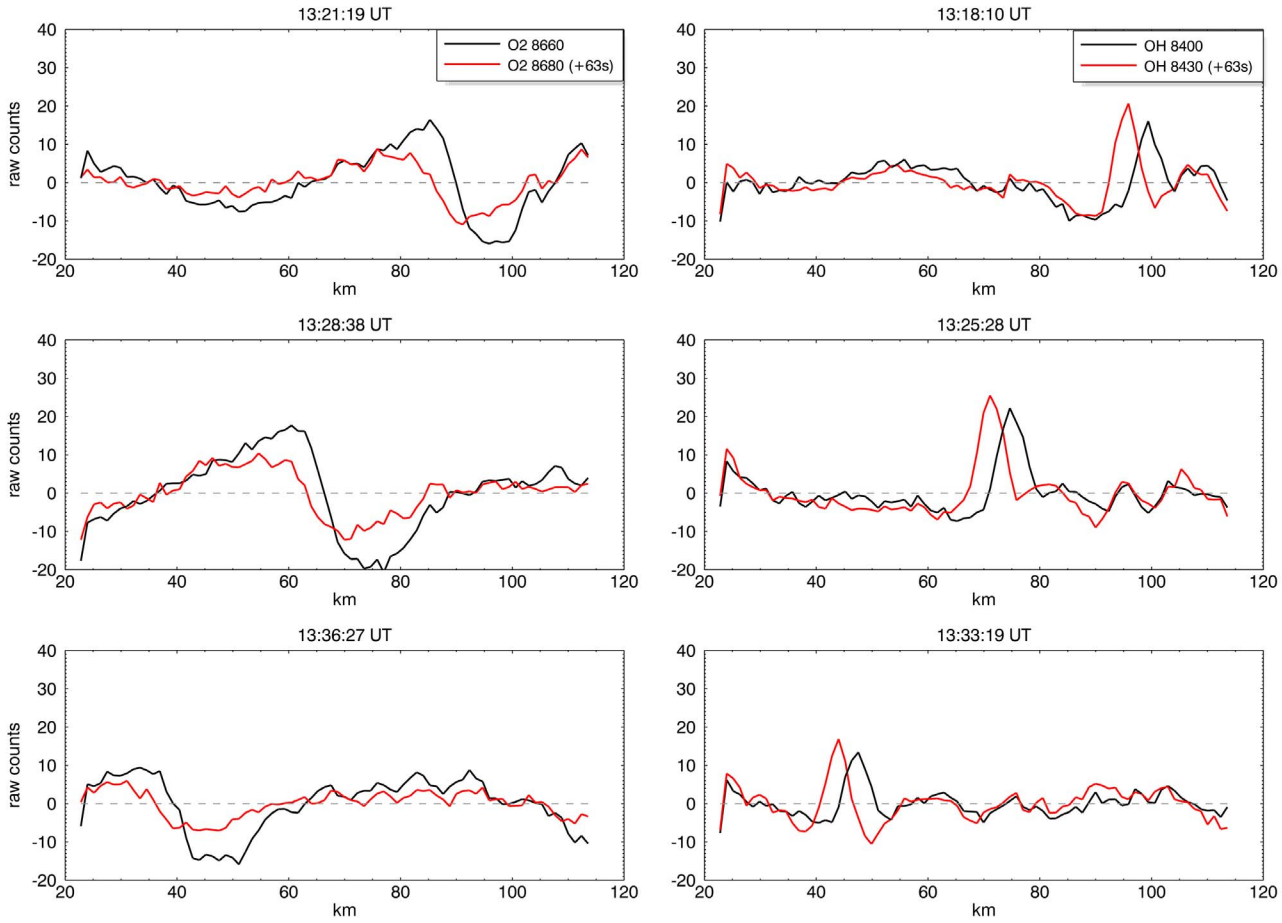


**Figure 4.** Line plots of the OHM and O2A brightness in two bands integrated along the wavefront, normal to the dashed lines in Figure 3. The origin for the abscissa is the intersection of the dashed lines and the image mask. A pixel dimension along the dashed lines is 0.7 km. The two plots in each row are separated in time by 63 s, with the 843 nm emission imaged later than the 840 nm emission, and the 868 nm emission later than the 866 nm. The wavefronts are the large peaks originally on the right of the plots. The waveforms are propagating from right to left. The data have been detrended with a quadratic polynomial fit.

after 13:00 UT. The decrease is about 20 K in OHM and is a similar amount in O2A. (The smaller value than those obtained from the images reflects the averaging.) The temperature then oscillates about a secular value which slowly decreases for OHM and remains nearly constant for O2A. In neither layer does the temperature show any tendency to recover to prepassage levels over the remainder of the night. Thus, the changes may be reasonable interpreted as a change in basic state. The temperature change occurs nearly in phase for the leading two oscillations; thereafter, the disturbance in O2A begins to lead the one in OHM until even later waves come into antiphase with each other. This indicates that the trailing waves are not fully ducted in the first instance and have a different modal structure from the leading waves in the second.

[18] A similar analysis for brightness (not shown) revealed the antiphase relation for the OHM and O2A emissions discussed earlier. The passage of the transition for preevent to postevent conditions occurred nearly simultaneously in temperature and brightness, with O2A and temperature having nearly the same phasing until the waves in the brightness became indistinct (after the first two or three waves).

## 3. Ducting

[19] Bores (or more generally long-lived horizontally propagating wave trains) require ducting to maintain the traveling disturbance [*Walterscheid and Hickey*, 2009; *Walterscheid et al.*, 1999; *Crook*, 1986; *Rottman and Grimshaw*, 2002]. Ducting in the free atmosphere is favored by a layer where the waves are internal surrounded by regions where the waves are external (evanescent), or nearly so. The approximate dispersion relation for gravity waves is

$$m^2 = \frac{N^2}{(c-\bar{u}_k)^2} - k^2 - \frac{1}{4H^2} \tag{1}$$

where $k$ is the horizontal wave number, $m$ is the vertical wave number, $N$ is the Brunt-Vaisala frequency, $c$ is the horizontal phase speed, $\bar{u}_k$ is the horizontal wind projected on the horizontal wave number vector and $H$ is the scale height. When

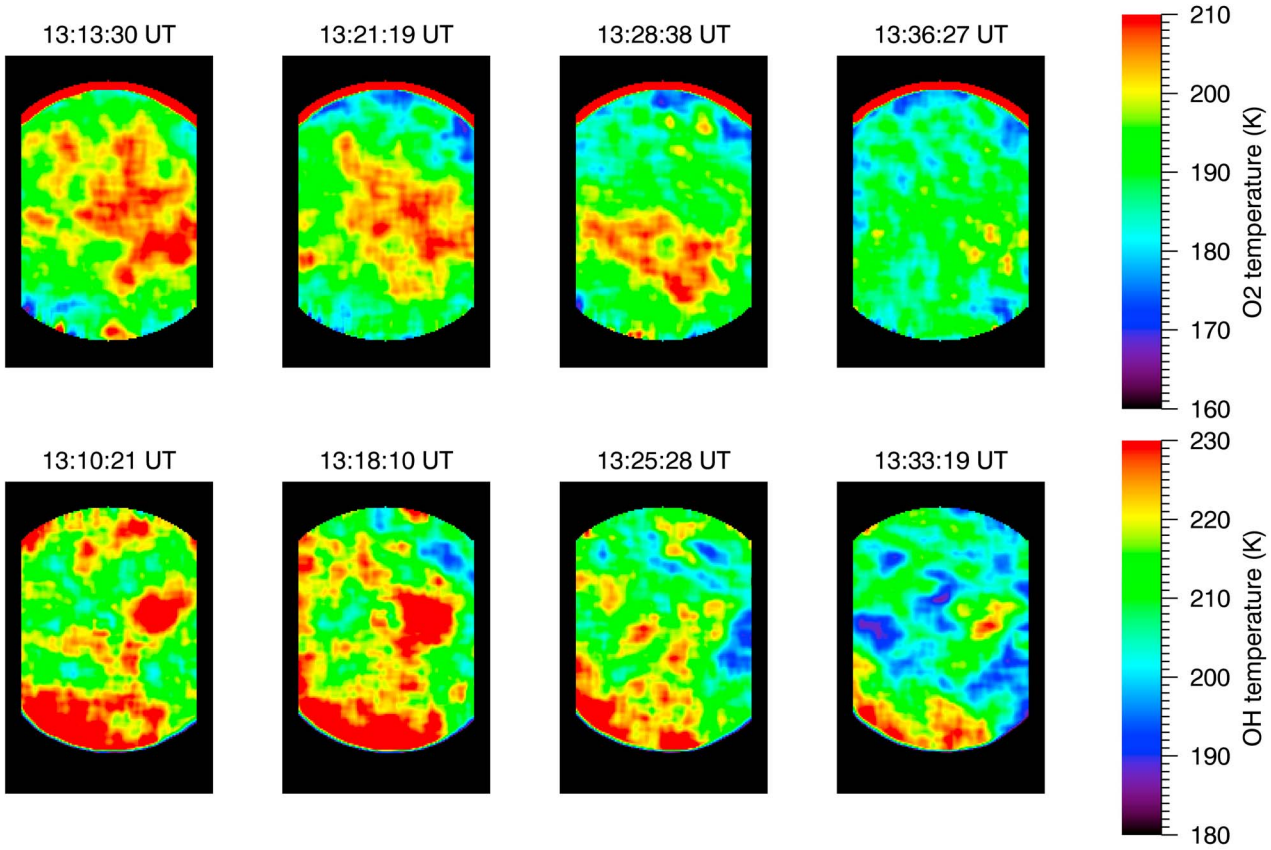


**Figure 5.** Maps of (top) O2A airglow temperature and (bottom) OHM temperature obtained from brightness pairs. The image size is 128 × 192 pixels (77 × 115 km). The black areas are where the image is masked to exclude edge effects.

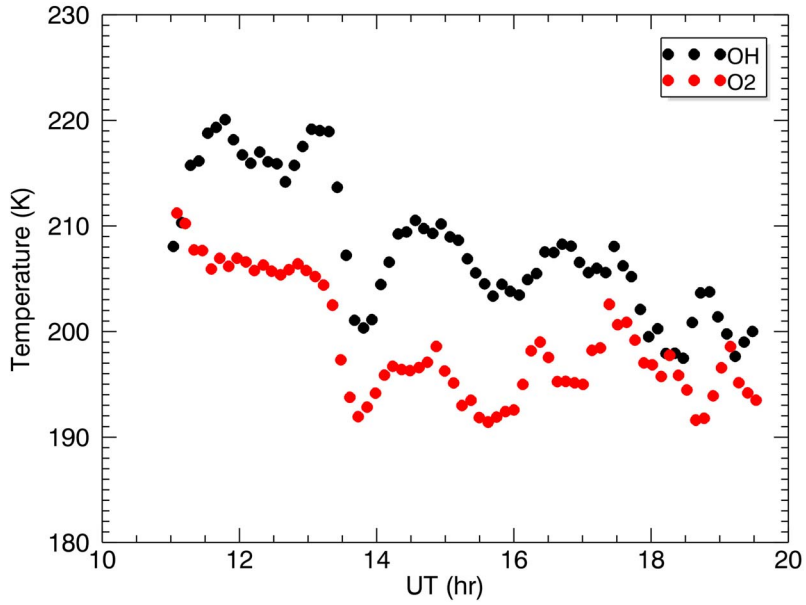


**Figure 6.** The time history of the temperature as the event passed the zenith. The temperature is averaged over the central 20 × 20 pixels (14 × 14 km) of the images. This gave a time history of the disturbance as it moved across the central part of the image with a time resolutions of 7 min. The times series were further smoothed by means of a three-point average.

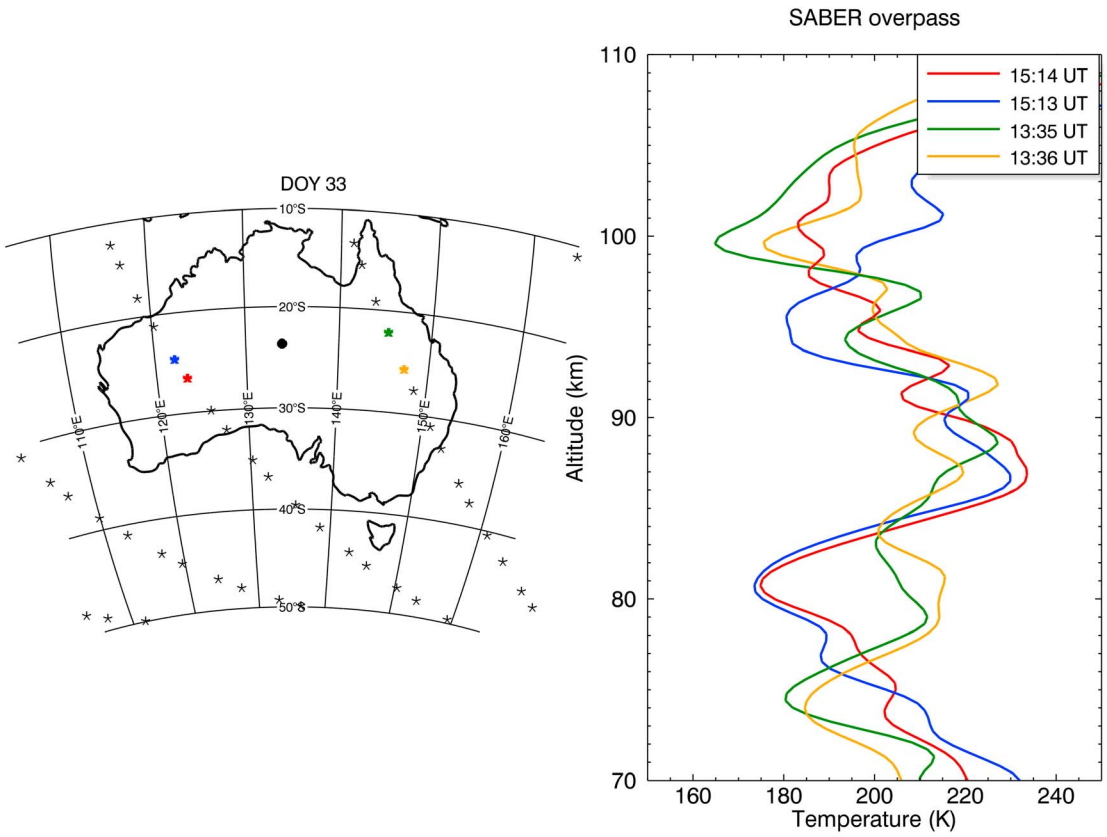


**Figure 7.** (left) The locations for the SABER profiles used for the basic state temperature profile. (right) The corresponding temperature profiles and times are shown in the upper right.

$m^2 > 0$, the waves are internal, and when $m^2 < 0$, they are external. From (1) it is inferred that evanescence is favored by winds opposed to the direction of wave propagation, short horizontal wavelengths and by low static stability. Ducting is also favored by reflection from gradients in $m^2$. Strong reflection is indicated when the WKB criterion is strongly violated or when [*Crook*, 1986; *Walterscheid et al.*, 2000; *Rottman and Grimshaw*, 2002]

$$\frac{1}{m}\frac{\partial m}{\partial z} \gg m \tag{2}$$

### 3.1. Simulations

[20] To assess the potential for ducting, we have performed calculations with a full wave model. The model and its application to ducting are described in detail by *Walterscheid and Hickey* [2009]. The model has been described by *Hickey et al.* [1997], *Walterscheid and Hickey* [2001], and *Schubert et al.* [2003]. Briefly, the full-wave model is a linear, steady state model that describes the vertical propagation of acoustic-gravity waves in an atmosphere with molecular viscosity and thermal conduction, ion drag, Coriolis force, and the eddy diffusion of heat and momentum in the mesosphere. The model solves the equations on a high-resolution vertical grid subject to boundary conditions and allows quite generally for propagation in a height varying atmosphere (nonisothermal mean state temperature and height varying mean winds and diffusion). The linearized equations are numerically integrated from the lower boundary to the upper boundary using the tridiagonal algorithm described by *Bruce et al.* [1953] and *Lindzen and Kuo* [1969]. The lower boundary is set well below the region of interest, and a sponge layer is implemented to avoid a large extraneous buildup of energy between the lower boundary and evanescent layers below any mesospheric ducts [e.g., *Walterscheid and Hickey*, 2009]. In this study the lower boundary (the bottom of the lower sponge layer) is placed 250 km below $z = 0$. The wave forcing is through the addition of heat in the energy equation. The heating is defined by a Gaussian profile with a full width at half maximum of 0.125 km. It is centered variously at an altitude of 10 km or 85 km. A Rayleigh-Newtonian sponge layer in addition to natural absorption by viscosity and heat conduction prevents spurious reflection from the upper boundary. At the upper boundary (here 300 km altitude) a radiation condition is imposed using a dispersion equation that includes dissipation [*Hickey and Cole*, 1987].

[21] The basic state temperature profile is a combination of temperatures derived from the NRLMSISE-00 model [*Picone et al.*, 2002] (hereafter denoted MSIS00) and the TIMED/SABER instrument [*Russell et al.*, 1999; http://gcmd.nasa.gov/records/GCMD_TIMED_SABER.html]. The SABER profile is an average of four profiles located over Australia for times before and after the observed wave event. Figure 7 (left) shows the locations for the SABER profiles used for the basic state temperature profile. Figure 7 (right)

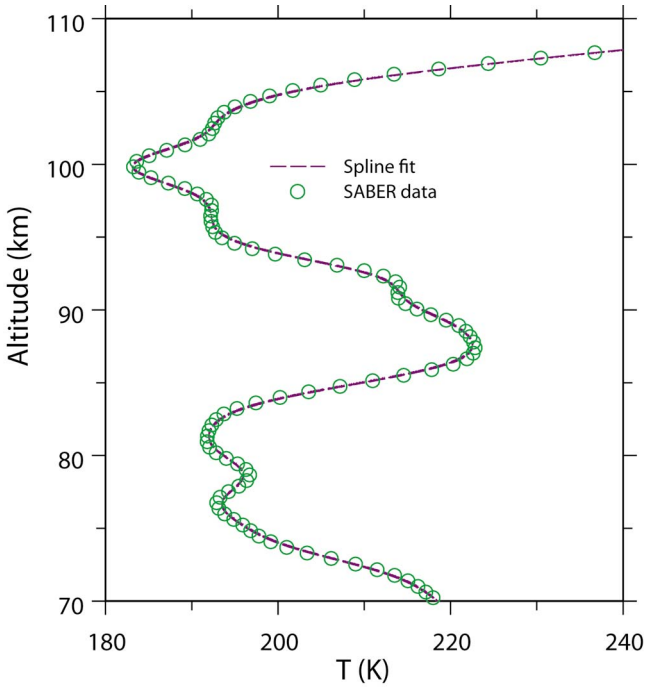


**Figure 8.** The temperature profile derived from the average of the TIMED/SABER data shown in Figure 7 as described in the text.

shows the corresponding temperature profiles along with the times.

[22] The model profile is obtained by first smoothing the SABER data over the altitude range 13 to 140 km with a five-point centered average, then smoothly joining this profile with the MSIS00 profile for the time and location of the observed event. The segment below the stratopause was modified as by *Walterscheid and Hickey* [2009] to prevent an extraneous buildup of energy in the stratosphere from unduly affecting the results in the upper mesosphere and lower thermosphere. A spline fit is performed over the entire profile. Figure 8 shows the temperature profile derived from the time and space averaging of the TIMED/SABER data described in the preceding paragraph and the fit to the vertically smoothed data.

[23] Figure 9 shows the profile of $N^2$ corresponding to the smoothed profile shown in Figure 8. There are distinct minima near 72 km and 94 km. Secondary minima are seen near 80 km and 90 km. A pronounced maximum is located near 85 km. Outside of the region bounded by the primary minima, $N^2$ increases. In the thermosphere the increase is not monotonic but takes place in a series of steps defined by local maxima and minima.

[24] The wind profile for the ducting calculations was derived by use of the Horizontal Wind Model version 2007 (HWM07) [*Drob et al.*, 2008] and data from the University of Adelaide Medium Frequency Doppler radar located at Buckland Park (34°38′S, 138°29′E) in South Australia [*Reid et al.*, 1995; *Holdsworth and Reid*, 2004; http://www.physics.adelaide.edu.au/atmospheric/mf.html]. The Alice Springs event occurred near the end of an episode of the phase locked 2 day wave (PL/TDW) [see *Hecht et al.*, 2010, Figure 3]. These events occur in the Southern Hemisphere summer and are characterized by large amplitudes and wave period tuned close to 48 h [*Walterscheid and Vincent*, 1996; *Hecht et al.*, 2010; *McCormack et al.*, 2010].

[25] The 2 day wave is not explicitly included in the HWM07. To account for the effect of the 2 day wave, we difference the Adelaide MF winds with the HWM07 winds for the time of the Alice Springs event and add this difference to the HWM winds for Alice Springs for the altitude region between 70 and 95 km. To avoid discontinuities in the profile, the PL/TDW wind difference is forced smoothly to zero at the upper and lower limits of the altitude region covered by the radar. We refer to the HWM07 winds for Alice Springs as the HWM winds and the PL/TDW modified winds as the HWM/TDW winds. This approach is justified by the fact that the PL/TWD is a hemispheric scale event and the scale of the PL/TDW far exceeds the distance between Adelaide and Alice Springs.

[26] Figure 10 shows the HWM and HWM/TDW winds projected on the direction of wave propagation. The magnitude and vertical extent of 2 day wave component agrees reasonably well with *Limpasuvan et al.* [2005] and *McCormack et al.* [2010]. The difference between the HWM and HWM/TDW profiles is substantial; the PL/TDW added approximately 50 m $s^{-1}$ to the HWM winds over the altitude range ~90 to 95 km. The effect of this is to decrease the intrinsic phase speed of the wave and to increase the vertical wave number (see (1)).

[27] The observations indicate a phase speed for the leading disturbance of ~54 m $s^{-1}$ and horizontal wavelength in the range 10–20 km. The lowest values are also more or less characteristic of the trailing waves, which tend to be somewhat slower. Figure 11 shows the vertical profiles of $m^2$ for a horizontal wavelength of 10 km based on the

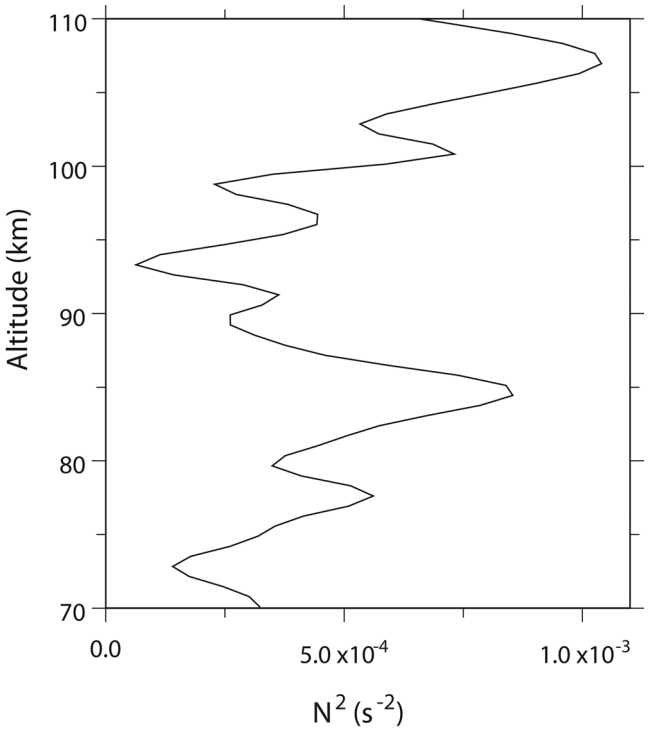


**Figure 9.** The profile of Brunt-Vaisala frequency derived from the temperature profile shown in Figure 8.

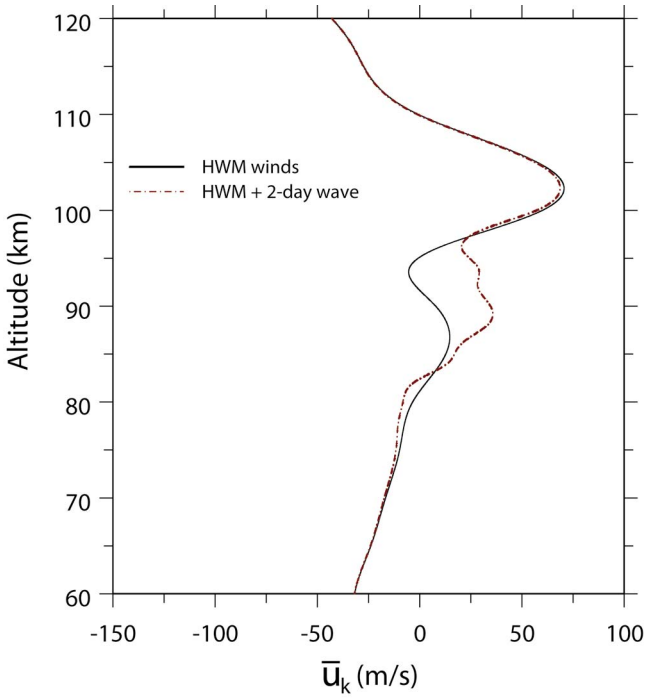


**Figure 10.** Model wind profiles obtained from the HWM07 model [*Drob et al.*, 2008] (solid curve) and by including a correction to the HWM07 winds using wind data from the Adelaide MF radar for the winds associated with a strong 2 day wave event as described in the text (dot-dashed curve). The winds have been projected on the direction of wave propagation so that positive values denote winds in the direction of wave propagation.

temperature and wind profiles shown in Figures 8 and 10, respectively. The rapid increase in $m^2$ to very large values above ~98 km is due to a critical level where the phase speed equals the projected wind speed. The values of $m^2$ for both wind profiles show large negative values of $m^2$ associated with the low values of $N^2$ in the upper mesosphere and near the steep lapse rates found near 93 km (see Figure 9). Maxima occur near 85 km in the HWM profile and near 88 km in the 2 day wave modified profile. The value of $m^2$ for both wind profiles is strongly evanescence below ~83 km. The difference between the maxima with and without the PL/TWD modified winds is pronounced. For the HWM winds there is a very limited region (~2 km in thickness) where $m^2 > 0$. With the effects of the PL/TDW wind the region where $m^2 > 0$ is far more extensive, extending from ~83 km to ~92 km.

[28] Figure 12 shows $m^2$ for the 20 km wave. The structure of the profiles is similar to those shown in Figure 11 but shifted to the right so that the altitude ranges for which $m^2 > 0$ are much greater, and the regions of evanescence are much reduced and much weaker. For the HWM profile the wave is internal from ~80 to 93 km. The altitude region over which the HWM/TDW profile is internal is similar, but the peak values of $m^2$are much larger. For the HWM/TDW profile the wave is only slightly evanescent in a limited altitude range above where $m^2 > 0$. However, low values of $m^2$ coupled with the steep gradient in $m^2$ above and below the minimum in the HWM/TDW profile suggest a high degree of reflection.

[29] Figure 13 shows the results of the full-wave model for the wave horizontal wind component $u'$ for a wave with a 10 km horizontal wavelength. Results are shown for the HWM and HWM/TDW profiles. The waves for both are forced at 85 km near where the $m^2$ profile for HWM has its maximum value. The forcing is adjusted to give a 5% fractional airglow response for the HWM/TDW profile. The same forcing is applied for HWM. The sharp local amplitude decrease at 85 km seen in both profiles is an artifact of the forcing. This is the only structure seen in the internal wave region for the HWM case. There is additional structure indicating standing wave behavior for the HWM/TDW case where $m^2 > 0$ (Figure 11). Over the main part of this region the response is much stronger in the HWM/TDW case than in the HWM case. At O2A altitudes (nominally ~90 km) the HWM/TDW response is weak and the HWM response is essentially nil.

[30] Figure 14 shows the disturbance wind response for a horizontal wavelength of 20 km. Again, the forcing is adjusted to give a 5% fractional airglow response for the HWM/TDW profile. As for 10 km horizontal wavelength, the HWM/TDW response is much stronger than the HWM case. The HWM response is significant in OH but is weak at O2A altitudes. The HWM/TDW response is large at both OHM and O2A altitudes. The structure for the HWM/TDW

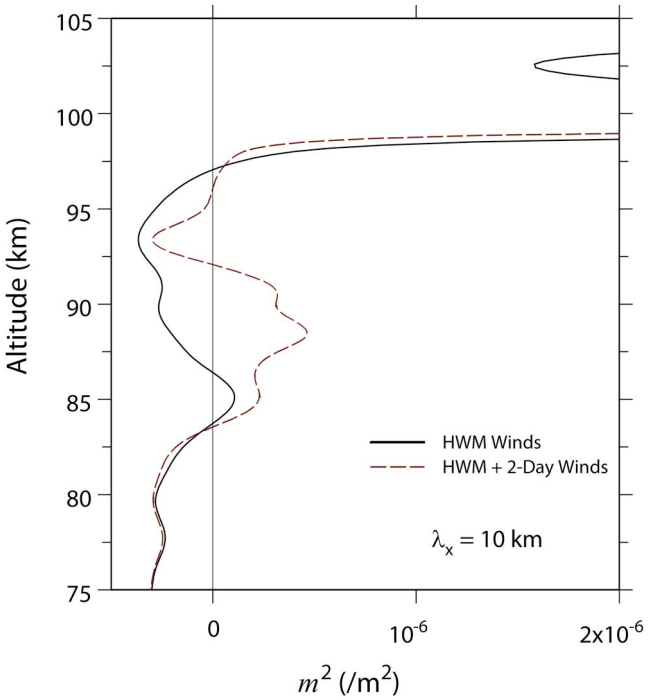


**Figure 11.** Vertical profiles of the vertical wave number squared based on the temperature and wind profiles shown in Figures 8 and 10, respectively. The profile is for a wave with a horizontal phase speed of 54 m s$^{-1}$ and a horizontal wavelength of 10 km. The profile denoted "HWM Winds" is based on HWM07 winds (solid curve) and the profile denoted "HWM + 2-Day Winds" is based on the wind profile modified for the presence of the phase-locked 2 day wave using Adelaide MF radar data (dashed curve).

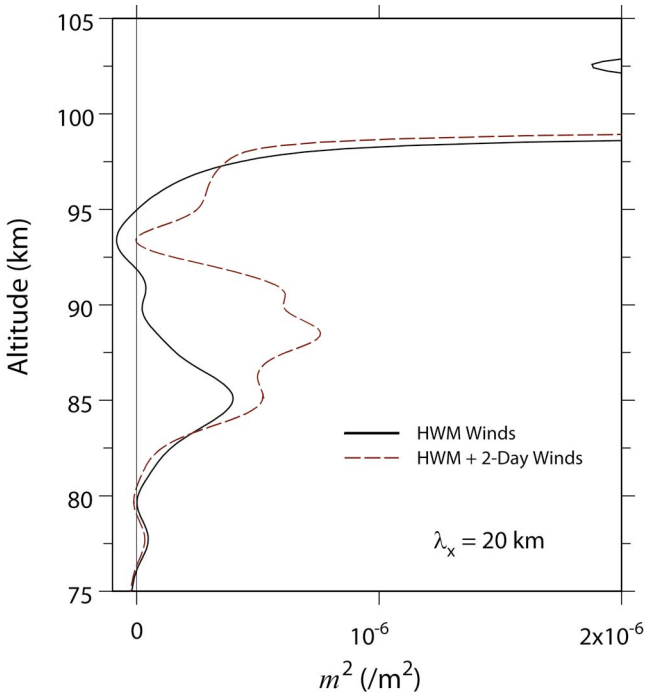


**Figure 12.** Same as Figure 11 but for a wave with a horizontal wavelength of 20 km.

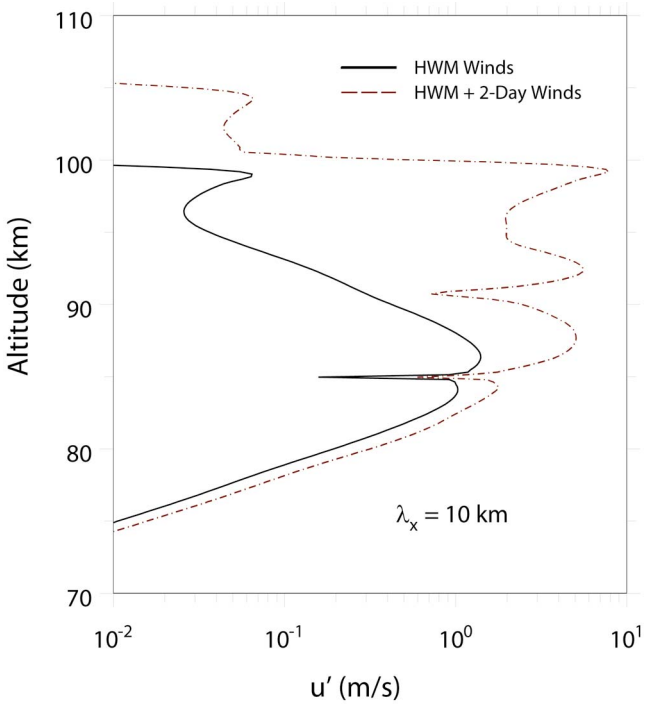


**Figure 13.** The amplitude profile of the horizontal velocity perturbation for a wave with a horizontal phase speed of 54 m $s^{-1}$ and a horizontal wavelength of 10 km and for a basic state that includes winds adjusted for the phase locked 2 day wave (dot-dashed curve) and a basic state where basic state winds are based entirely on climatology (solid).

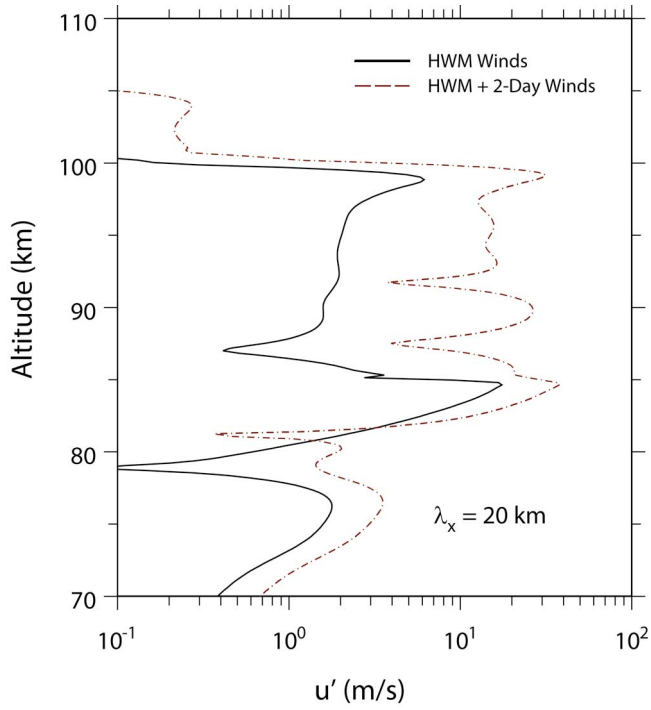


**Figure 14.** Same as Figure 13 but for a wave with a horizontal wavelength of 20 km.

case indicates standing wave behavior for altitudes where $m^2 > 0$ (Figure 11). The response in both layers is much greater for the 20 km horizontal wavelength than for 10 km.

[31] We examined the wave response for horizontal wavelengths in the range 15–20 km to see where the response was a maximum. Since the horizontal phase speed was well constrained, we fixed it at $c$ = 54 m $s^{-1}$. The horizontal wavelength was varied in steps of 0.01 km. The forcing was the same for all values of horizontal wavelength. The measure of the response was the vertically integrated kinetic energy in the altitude region 82 to 87 km, corresponding to the amplitude feature peaking near 84 km (Figure 14) [*Walterscheid and Hickey*, 2009]. The results are shown in Figure 15. There is a clear kinetic energy peak near 19 km.

[32] The results of the full-wave calculations for a horizontal wavelength of 19 km are shown in Figure 16. The results are similar to those shown in Figure 14 for the 20 km wavelength except that the difference in amplitude between the HWM and HWM/TDW cases is much greater as result of the HWM results being much weaker. The fact that the HWM/TDW results are similar in amplitude to the 20 km case is a consequence of the fact that in both cases the forcing is adjusted to give a 5% fractional OHM airglow response.

### 3.2. Nonlinearity

[33] The ratio of the front speed to the wave speed defines a Froude number

$$F = \frac{U_k}{c} \tag{3}$$

where $U_k$ is the current speed in the direction of **k** in the upstream region where the wave formed [*White and*

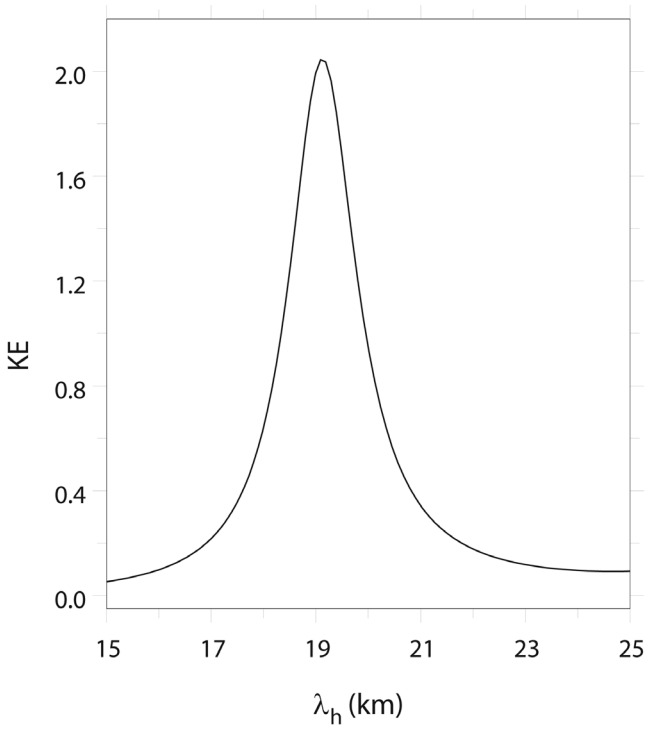


**Figure 15.** The vertically integrated kinetic energy over the altitude region 82 to 87 km as a function of horizontal wavelength. The horizontal phase speed is 54 m $s^{-1}$.

*Helfrich*, 2008]. Values of $F$ close to unity imply a significant degree of nonlinearity. A characteristic of nonlinearity is amplitude ordering with each successive wave behind the front having smaller amplitude than the one before it [*Christie*, 1989]. The amplitude decrease can be gradual. Supercritical bores ($F > 1$) may have a waveform consisting of a large leading disturbance followed by weak trailing waves [*Melville and Helfrich*, 1987; *Helfrich and Melville*, 2006]. For the event we examine, $F$ determined locally is somewhat less than unity but may well be supercritical upstream. The waveform seen in the OHM airglow shown in Figure 6 (a large leading disturbance followed by weak trailing waves) might therefore reflect supercriticality. The amplitudes of successive trailing waves show no discernible amplitude ordering, though this could be an observational artifact of the weakness of the waves.

## 4. Discussion

[34] We have analyzed a dramatic wave event seen in the airglow over Alice Springs, Australia. The event shows conditions associated with events elsewhere that have been interpreted as bores [*Smith et al.*, 2003, 2005; *Dewan and Picard*, 1998; *Nielsen et al.*, 2006]. These conditions are a wave train following a moving front in airglow intensity and a change in temperature behind the front. Also indicative is the opposite response of the airglow in the OHM and O2A layers, with a dramatic brightening in the former and darkening in the latter [*Smith et al.*, 2003, 2005; *Dewan and Picard*, 1998; *Nielsen et al.*, 2006].

[35] A necessary condition for a bore interpretation is significant wave trapping [*Crook*, 1986; *Rottman and Grimshaw*, 2002]. We have analyzed the ducting for the event using a combination of empirical models (MSIS00 and HWM07) and data (Adelaide MF radar winds and TIMED/SABER temperature data). During the wave event an instance of the PL/TDW was underway [*Hecht et al.*, 2010]. We find significant trapping in the vicinity of the airglow layers that was greatly enhanced by the winds associated with the PL/TDW. It seems unlikely that the event would have occurred were it not for the PL/TDW-induced winds.

[36] We have also examined the possibility that PL/TDW thermal structure played a role in the event. A comparison between the thermal structure inferred from TIMED/SABER and MSIS for the time and place of the event (not shown) indicated that MSIS00 did not exhibit the structure in the upper mesosphere that gave the low values of the Brunt-Vaisala frequency necessary for wave ducting. One cannot attribute the difference between the MSIS00 values and the observed values entirely to the PL/TDW, but it appears likely that PL/TDW-induced thermal structure played a role in the necessary ducting.

[37] Values near 20 km were characteristic of the major leading disturbance in the O2A layer. The isolated leading disturbance in the OHM layer had a horizontal scale of ~10 km. Including the comparatively dim feature preceding the large bright feature gives ~20 km. Calculations (Figure 16) indicate that values near 20 km are consistent with a resonant response near a horizontal wavelength of 19 km. Another region of resonance (not shown) corresponding to a faster lower-order mode occurs for phase speeds near 85 m $s^{-1}$. The weak trailing waves are consistent with a subdued

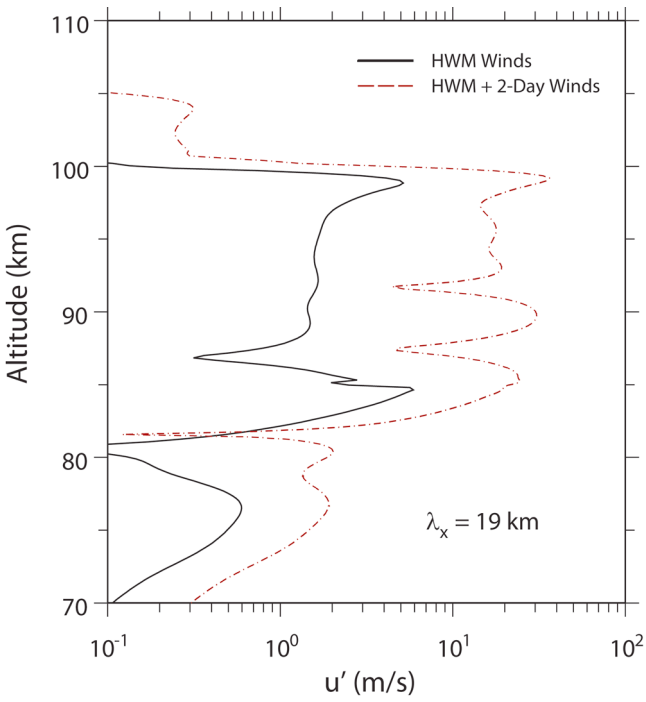


**Figure 16.** Same as Figure 13 but for a wave with a horizontal wavelength of 19 km.

response for wavelengths ~10 km compared to the strong near resonant response near 20 km.

[38] The leading disturbance in the OHM airglow was (except for the weak trailing waves) an isolated disturbance associated with frontal-like behavior indicative of a horizontally propagating ducted wave train that has acquired maximum amplitude at its leading edge. This behavior suggests a bore whose leading disturbances is a solitary wave [*Dewan and Picard*, 1998; *Smith et al.*, 2003, 2005, 2006; *Rottman and Einaudi*, 1993]. A solitary wave followed by a train of weak trailing waves indicates a fairly large degree of nonlinearity [*Rottman and Einaudi*, 1993]. The observations indicated that the degree of nonlinearly where the waves were observed was marginal, but we cannot rule out a high degree of nonlinearity where the wave was produced.

[39] The temperature change in both layers is characterized by cooling across the moving front of ~25 K for O2A and ~30 K for OHM. This is the first work of which we are aware that reports an extensive change in temperature across the front. The change in temperature suggests a change in the basic state across the moving front and agrees with the idea that a bore is a wave transition between basic states [*Grimshaw*, 2002]. What instigates this change is not clear.

[40] One possibility is a lower atmosphere source for the event. The evanescence at the bottom of the duct is not strong. It is possible that the bore-like event could have originated in a large-amplitude upward propagating wave with a phase speed and wavelength not too different from those consistent with a resonant wave. Once the wave gained access to the ducting, it is possible that the energy was transferred to the nearby resonance by nonlinear processes [*Christie*, 1989; *Grimshaw et al.*, 2002; *Knupp*, 2006; *Rottman and Einaudi*, 1993; *Rottman and Grimshaw*, 2002; *Young et al.*, 1994]. This interpretation is supported by the fact that the lower-order mode with the faster phase speed is not seen. The lower-order mode has a higher degree of evanescence on the bottom side and presents a greater barrier to upward propagation. Calculations for waves forced from below (not shown) give a much smaller amplitude in the airglow region for the resonance corresponding to phase speeds ~85 km than with the observed phase speeds. If the wave is forced from below, then the change in the basic state temperature across the front may be regarded as a consequence of the action of gravity waves in extracting heat from the region [*Walterscheid*, 1981; *Hickey et al.*, 2011].

[41] Another possibility is that the cooler temperatures behind the front indicate some lifting. This might be caused by a current flowing along a sloping stable layer, forced perhaps by some combination of tidal and planetary wave (e.g., the PL/TDW) action [*Flynn and Sutherland*, 2004; *Knupp*, 2006]. *Dewan and Picard* [1998] have suggested a tidal mechanism.

[42] There can be longer-period features (~ hour period waves) associated with frontal events that might play a formative role in frontal events, such as the one studied by *Li et al.* [2007]. The occurrence of the Alice Springs event toward the end of the PL/TDW wave might be explained by conditions that allow propagation of slower gravity waves to mesospheric altitudes as the PL/TDW weakens. Here we have examined the wave features revealed in the images that are integral to the event and more or less characteristic of waves seen in association with frontal events [*Smith et al.*, 2005, 2006; *Stockwell et al.*, 2006; *Taylor et al.*, 1995a].

[43] The weak wave train following the front suggests the possibility that waves are not the only mechanism responsible for removing excess kinetic energy generated at the bore front. Indeed, when a degree of nonlinearity is involved (as in a bore or a cnoidal wave train) the energy carried back relative to the crests cannot account for all of the excess energy that needs to be depleted [*Lighthill*, 1978]. Some energy might be depleted by vertical leakage from the duct. In addition, a reasonable alternative to a pure undular bore is a mixed bore that is partly turbulent [*Lighthill*, 1978]. At the front, mixing would bring down atomic oxygen which would enhance the OHM emission through $O_3$ production and diminish the O2A emission by diminishing production [*Hecht et al.*, 1995]. This would account for the observed brightening of the OHM airglow emission and the dimming of the O2A airglow.

## 5. Conclusions

[44] We have analyzed a case of a dramatic frontal event observed over Alice Springs, Australia. The major findings are as follows:

[45] 1. The event is most likely a bore or a train of nonlinear (cnoidal) waves. The large isolated leading disturbance in the OHM airglow suggests the possibility that the leading disturbance is a solitary wave.

[46] 2. The event has characteristics of an undular bore, but the trailing waves are very weak suggesting the possibility that turbulence as well as wave transport is removing excess energy generated at the moving front.

[47] 3. Calculations indicate that the PL/TDW occurring at the time was an essential contributor to the ducting required to maintain a wave train at airglow altitudes.

[48] 4. The OHM and O2A airglow brightness behind the front was among the brightest for Alice Springs that we have measured in 7 years of observations.

[49] **Acknowledgments.** R.L.W., L.J.G. and J.H.H. acknowledge support from NSF grants AGS-1001086, AGS-1042259, and ATM-0737557 and from NASA grant NNX11AH82G. I.M.R. acknowledges support from ARC grants DP0878114 and DP1096901. M.P.H. acknowledges support from NSF grant AGS-1001074. We gratefully acknowledge the SABER Team for producing the temperature profiles used in the calculations.

## References

Batista, P. P., B. R. Clemesha, D. M. Simonich, M. J. Taylor, H. Takahashi, D. Gobbi, I. S. Batista, R. A. Buriti, and A. F. Medeiros (2002), Simultaneous lidar observation of a sporadic sodium layer, a "wall" event in the OH and OI5577 airglow images and the meteor winds, *J. Atmos. Sol. Terr. Phys.*, *64*, 1327–1335, doi:10.1016/S1364-6826(02)00116-5.

Brown, L. B., A. J. Gerrard, J. W. Meriwether, and J. J. Makela (2004), All-sky imaging observations of mesospheric fronts in OI 557.7 nm and broadband OH airglow emissions: Analysis of frontal structure, atmospheric background conditions, and potential sourcing mechanisms, *J. Geophys. Res.*, *109*, D19104, doi:10.1029/2003JD004223.

Bruce, G. H., D. W. Peaceman, H. H. Rachford Jr., and J. D. Rice (1953), Calculations of unsteady-state gas flow through porous media, *J. Pet. Technol.*, *198*, 79–92.

Christie, D. R. (1989), Long nonlinear waves in the lower atmosphere, *J. Atmos. Sci.*, *46*, 1462–1491, doi:10.1175/1520-0469(1989)046<1462:LNWITL>2.0.CO;2.

Crook, N. A. (1986), The effect of ambient stratification and moisture on the motion of atmospheric undular bores, *J. Atmos. Sci.*, *43*, 171–181, doi:10.1175/1520-0469(1986)043<0171:TEOASA>2.0.CO;2.

Dewan, E. M., and R. H. Picard (1998), Mesospheric bores, *J. Geophys. Res.*, *103*, 6295–6305, doi:10.1029/97JD02498.

Drob, D. P., et al. (2008), An empirical model of the Earth's horizontal wind fields: HWM07, *J. Geophys. Res.*, *113*, A12304, doi:10.1029/2008JA013668.

Fechine, J., A. F. Medeiros, R. A. Buriti, H. Takahashi, and D. Gobbi (2005), Mesospheric bore events in the equatorial middle atmosphere, *J. Atmos. Sol. Terr. Phys.*, *67*, 1774–1778, doi:10.1016/j.jastp.2005.04.006.

Fechine, J., et al. (2009), First observation of an undular mesospheric bore in a Doppler duct, *Ann. Geophys.*, *27*, 1399–1406, doi:10.5194/angeo-27-1399-2009.

Flynn, M. R., and B. R. Sutherland (2004), Intrusive gravity currents and internal gravity wave generation in stratified fluid, *J. Fluid Mech.*, *514*, 355–383.

Gelinas, L. J., J. H. Hecht, R. L. Walterscheid, R. G. Roble, and J. M. Woithe (2008), A seasonal study of mesospheric temperatures and emission intensities at Adelaide and Alice Springs, *J. Geophys. Res.*, *113*, A01304, doi:10.1029/2007JA012587.

Grimshaw, R. H. J. (2002), Internal solitary waves, in *Environmental Stratified Flows, Topics Environ. Fluid Mechanics*, vol. 3, edited by R. Grimshaw, pp. 1–29, Kluwer Acad., Dordrecht, Netherlands.

Grimshaw, R. H. J., K. H. Chan, and K. W. Chow (2002), Transcritical flow of a stratified fluid: The forced extended Korteweg-de Vries model, *Phys. Fluids*, *14*, 755–774, doi:10.1063/1.1429962.

Hecht, J. H., R. L. Walterscheid, and M. N. Ross (1994), First measurements of the two-dimensional horizontal wavenumber spectrum from CCD images of the nightglow, *J. Geophys. Res.*, *99*, 11,449–11,460, doi:10.1029/94JA00584.

Hecht, J. H., S. K. Ramsay Howat, R. L. Walterscheid, and J. R. Isler (1995), Observations of variations in the OH Meinel nightglow during ALOHA 93, *Geophys. Res. Lett.*, *22*, 2817–2820, doi:10.1029/95GL03019.

Hecht, J. H., R. L. Walterscheid, D. C. Fritts, J. R. Isler, D. C. Senft, C. S. Gardner, and S. J. Franke (1997), Wave breaking signatures in OH airglow and sodium densities and temperatures. Airglow imaging, Na lidar, and MF radar observations, *J. Geophys. Res.*, *102*, 6655–6668, doi:10.1029/96JD02619.

Hecht, J. H., R. L. Walterscheid, M. P. Hickey, and S. J. Franke (2001), Climatology and modeling of quasi-monochromatic atmospheric gravity waves observed over Urbana, Illinois, *J. Geophys. Res.*, *106*, 5181–5195, doi:10.1029/2000JD900722.

Hecht, J. H., S. Kovalam, P. T. May, G. Mills, R. A. Vincent, R. L. Walterscheid, and J. Woithe (2004), Airglow imager observations of atmospheric gravity waves at Alice Springs and Adelaide, Australia, during the Darwin Area Wave Experiment (DAWEX), *J. Geophys. Res.*, *109*, D20S05, doi:10.1029/2004JD004697.

Hecht, J. H., R. L. Walterscheid, L. J. Gelinas, R. A. Vincent, I. M. Reid, and J. M. Woithe (2010), Observations of the phase-locked 2 day wave over the Australian sector using medium-frequency radar and airglow data, *J. Geophys. Res.*, *115*, D16115, doi:10.1029/2009JD013772.

Helfrich, K. R., and W. K. Melville (2006), Long nonlinear waves, *Annu. Rev. Fluid Mech.*, *38*, 395–425, doi:10.1146/annurev.fluid.38.050304.092129.

Hickey, M. P., and K. D. Cole (1987), A quartic dispersion equation for internal gravity waves in the thermosphere, *J. Atmos. Terr. Phys.*, *49*, 889–899, doi:10.1016/0021-9169(87)90003-1.

Hickey, M. P., R. L. Walterscheid, M. J. Taylor, W. Ward, G. Schubert, Q. Zhou, F. Garcia, M. C. Kelley, and G. G. Shepherd (1997), Numerical simulations of gravity waves imaged over Arecibo during the 10-day January 1993 campaign, *J. Geophys. Res.*, *102*, 11,475–11,489, doi:10.1029/97JA00181.

Hickey, M. P., R. L. Walterscheid, and G. Schubert (2011), Gravity wave heating and cooling of the thermosphere: Sensible heat flux and viscous flux of kinetic energy, *J. Geophys. Res.*, *116*, A12326, doi:10.1029/2011JA016792.

Holdsworth, D. A., and I. M. Reid (2004), The Buckland Park MF Radar: Final implementation, observation schemes and velocity comparisons, *Ann. Geophys.*, *22*, 3815–3828, doi:10.5194/angeo-22-3815-2004.

Knupp, K. R. (2006), Observational analysis of a gust front to bore to solitary wave transition within an evolving nocturnal boundary layer, *J. Atmos. Sci.*, *63*, 2016–2035, doi:10.1175/JAS3731.1.

Li, F., G. R. Swenson, A. Z. Liu, M. Taylor, and Y. Zhao (2007), Investigation of a "wall" wave event, *J. Geophys. Res.*, *112*, D04104, doi:10.1029/2006JD007213.

Lighthill, J. (1978), *Waves in Fluids*, 504 pp., Cambridge Univ. Press, Cambridge, U. K.

Limpasuvan, V., D. L. Wu, M. J. Schwartz, J. W. Waters, Q. Wu, and T. L. Killeen (2005), The two-day wave in EOS MLS temperature and wind measurements during 2004–2005 winter, *Geophys. Res. Lett.*, *32*, L17809, doi:10.1029/2005GL023396.

Lindzen, R. S., and H. L. Kuo (1969), A reliable method for the numerical integration of a large class of ordinary and partial differential equations, *Mon. Weather Rev.*, *97*, 732–734, doi:10.1175/1520-0493(1969)097<0732:ARMFTN>2.3.CO;2.

McCormack, J. P., S. D. Eckermann, K. W. Hoppel, and R. A. Vincent (2010), Amplification of the quasi-two day wave through nonlinear interaction with the migrating diurnal tide, *Geophys. Res. Lett.*, *37*, L16810, doi:10.1029/2010GL043906.

Medeiros, A., J. Fechine, R. Buriti, H. Takahashi, C. Wrasse, and D. Gobbi (2005), Response of OH, $O_2$ and OI5577 airglow emissions to the mesospheric bore in the equatorial region of Brazil, *Adv. Space Res.*, *35*, 1971–1975, doi:10.1016/j.asr.2005.03.075.

Melville, W. K., and K. R. Helfrich (1987), Transcritical flow over topography, *J. Fluid Mech.*, *178*, 31–52, doi:10.1017/S0022112087001101.

Narayanan, V. L., S. Gurubaran, and K. Emperumal (2009), A case study of a mesospheric bore event observed with an all-sky airglow imager at Tirunelveli (8.7°N), *J. Geophys. Res.*, *114*, D08114, doi:10.1029/2008JD010602.

Nielsen, K., M. J. Taylor, R. Stockwell, and M. Jarvis (2006), An unusual mesospheric bore event observed at high latitudes over Antarctica, *Geophys. Res. Lett.*, *33*, L07803, doi:10.1029/2005GL025649.

Picone, J. M., A. E. Hedin, D. P. Drob, and A. C. Aikin (2002), NRLMSISE-00 empirical model of the atmosphere: Statistical comparisons and scientific issues, *J. Geophys. Res.*, *107*(A12), 1468, doi:10.1029/2002JA009430.

Reid, I. M., B. G. W. Vandepeer, S. C. Dillon, and B. M. Fuller (1995), The new Adelaide medium frequency Doppler radar, *Radio Sci.*, *30*(4), 1177–1189, doi:10.1029/95RS00731.

Rottman, J. W., and F. Einaudi (1993), Solitary waves in the atmosphere, *J. Atmos. Sci.*, *50*, 2116–2136, doi:10.1175/1520-0469(1993)050<2116:SWITA>2.0.CO;2.

Rottman, J. W., and R. Grimshaw (2002), Atmospheric internal solitary waves, in *Environmental Stratified Flows, Topics Environ. Fluid Mech.*, vol. 3, edited by R. Grimshaw, pp. 61–88, Springer, New York.

Russell, J. M., III, M. G. Mlynczak, L. L. Gordley, J. Tansock, and R. Esplin (1999), An overview of the SABER experiment and preliminary calibration results, paper presented at the SPIE 44th Annual Meeting, Denver, Colo., 18–23 July.

Scheer, J., and E. R. Reisin (2010), Statistical properties of nonlinear wave signatures in OH and $O_2$ airglow brightness data observed at lower midlatitudes, *J. Atmos. Sol. Terr. Phys.*, *72*, 588–594, doi:10.1016/j.jastp.2010.02.015.

Schubert, G., M. P. Hickey, and R. L. Walterscheid (2003), Heating of Jupiter's thermosphere by the dissipation of upward propagating acoustic waves, *Icarus*, *163*, 398–413, doi:10.1016/S0019-1035(03)00078-2.

She, C. Y., T. Li, B. P. Williams, T. Yuan, and R. H. Picard (2004), Concurrent OH imager and sodium temperature/wind lidar observation of a mesopause region undular bore event over Fort Collins/Platteville, Colorado, *J. Geophys. Res.*, *109*, D22107, doi:10.1029/2004JD004742.

Smith, S. M., M. J. Taylor, G. R. Swenson, C.-Y. She, W. Hocking, J. Baumgardner, and M. Mendillo (2003), A multidiagnostic investigation of the mesospheric bore phenomenon, *J. Geophys. Res.*, *108*(A2), 1083, doi:10.1029/2002JA009500.

Smith, S. M., J. Friedman, S. Raizada, C. Tepley, J. Baumgardner, and M. Mendillo (2005), Evidence of mesospheric bore formation from a breaking gravity wave event: Simultaneous imaging and lidar measurements, *J. Atmos. Sol. Terr. Phys.*, *67*, 345–356, doi:10.1016/j.jastp.2004.11.008.

Smith, S. M., J. Sheer, S. Raizada, E. Reisin, J. Baumgardner, and M. Mendillo (2006), Characterization of exceptionally strong mesospheric wave event using all-sky and zenith airglow observations, *J. Geophys. Res.*, *111*, A09309, doi:10.1029/2005JA011197.

Snively, J. B., V. P. Pasko, and M. J. Taylor (2010), OH and OI airglow layer modulation by ducted short-period gravity waves: Effects of trapping altitude, *J. Geophys. Res.*, *115*, A11311, doi:10.1029/2009JA015236.

Stockwell, R., M. J. Taylor, K. Nielsen, and M. A. Jarvis (2006), A novel joint space-wavenumber analysis of an unusual Antarctic gravity wave event, *Geophys. Res. Lett.*, *33*, L08805, doi:10.1029/2005GL025660.

Swenson, G. R., J. Qian, J. M. C. Plane, P. J. Epsy, M. J. Taylor, D. N. Turnbull, and R. P. Lowe (1998), Dynamical and chemical aspects of the mesospheric Na "wall" event on October 9, 1993 during the airborne lidar and observations of Hawaiian airglow (ALOHA) campaign, *J. Geophys. Res.*, *103*, 6361–6380, doi:10.1029/97JD03379.

Taylor, M. J., D. N. Turnbull, and R. P. Lowe (1995a), Spectrometric and imaging measurements of a spectacular gravity wave event observed during the ALOHA-93 campaign, *Geophys. Res. Lett.*, *22*, 2849–2852, doi:10.1029/95GL02948.

Taylor, M. J., D. C. Fritts, and J. R. Isler (1995b), Determination of horizontal and vertical structure of an unusual pattern of short period gravity waves imaged during ALOHA-93, *Geophys. Res. Lett.*, *22*, 2837–2840, doi:10.1029/95GL02945.

Walterscheid, R. L. (1981), Dynamical cooling induced by dissipating internal gravity waves, *Geophys. Res. Lett.*, *8*, 1235–1238, doi:10.1029/GL008i012p01235.

Walterscheid, R. L., and M. P. Hickey (2001), One-gas models with height-dependent mean molecular weight: Effects on gravity wave propagation, *J. Geophys. Res.*, *106*, 28,831–28,839, doi:10.1029/2001JA000102.

Walterscheid, R. L., and M. P. Hickey (2009), Gravity wave ducting in the upper mesosphere and lower thermosphere duct system, *J. Geophys. Res.*, *114*, D19109, doi:10.1029/2008JD011269.

Walterscheid, R. L., and R. A. Vincent (1996), Tidal generation of the phase-locked 2-day wave in the southern hemisphere summer by wave-wave interactions, *J. Geophys. Res.*, *101*(D21), 26,567–26,576, doi:10.1029/96JD02248.

Walterscheid, R. L., J. H. Hecht, R. A. Vincent, I. M. Reid, J. Woithe, and M. P. Hickey (1999), Analysis and interpretation of airglow and radar observations of quasi-monochromatic gravity waves in the upper mesosphere and lower thermosphere over Adelaide, Australia (35°S, 138°E), *J. Atmos. Sol. Terr. Phys.*, *61*, 461–478, doi:10.1016/S1364-6826(99)00002-4.

Walterscheid, R. L., J. H. Hecht, F. T. Djuth, and C. A. Tepley (2000), Evidence of reflection of a long-period gravity wave in observations of the nightglow over Arecibo on May 8–9 1989, *J. Geophys. Res.*, *105*, 6927–6934, doi:10.1029/1999JD901065.

White, B. L., and K. R. Helfrich (2008), Gravity currents and internal waves in a stratified fluid, *J. Fluid Mech.*, *616*, 327–356, doi:10.1017/S0022112008003984.

Young, R. E., R. L. Walterscheid, G. Schubert, L. Pfister, H. Houben, and D. L. Bindschadler (1994), Characteristics of finite amplitude stationary gravity waves in the atmosphere of Venus, *J. Atmos. Sci.*, *51*, 1857–1875, doi:10.1175/1520-0469(1994)051<1857:COFASG>2.0.CO;2.

Zhang, S. P., and G. G. Shepherd (1999), The influence of the diurnal tide on the O ($^1$S) and OH emission rates observed by WINDII on UARS, *Geophys. Res. Lett.*, *26*, 529–532, doi:10.1029/1999GL900033.